RSC Advances

PAPER

Cite this: *RSC Adv.*, 2019, **9**, 42228

Er^{3+}/Yb^{3+} co-doped nanocrystals modified with 6-aminocaproic acid for temperature sensing in biomedicine†

Bing Wu, [a] Lijuan Zhao,*[a] Ying Wang,[b] Haotian Dong[a] and Hua Yu*[a]

Received 16th October 2019
Accepted 4th December 2019

DOI: 10.1039/c9ra08447a

rsc.li/rsc-advances

We report β-PbF_2:Er^{3+}/Yb^{3+} nanocrystals (NCs) modified with 6-aminocaproic acid (6AA) *via* wet chemical etching of glass ceramics (GCs). NCs body-doped with trivalent rare-earth (RE^{3+}) ions were released from the GCs by etching of the glass matrix and modified with bifunctional 6AA ligands to enhance their water solubility. They have good stability in water with an average diameter of 56 nm and display efficient green (521, 550 nm) and red (660 nm) emission under the excitation of a 940 nm laser. High absolute sensitivity (S_A) and relative sensitivity (S_R) (0.0027 K^{-1} and 1.18% K^{-1}, respectively) and high resolution (0.25 K) were achieved for temperature sensing in the biological temperature range, using the fluorescence intensity ratio (FIR) technique. All of the experimental results indicate that the Er^{3+}/Yb^{3+} co-doped NCs modified with 6AA may potentially be useful as fluorescent biological temperature sensors.

Introduction

Temperature is a key parameter in many fields, including medicine, aeronautics, electronics, and catalysis.[1,2] Conventional contact temperature measurements are based on the principle of either the thermal expansion of materials or the Seebeck effect, for example liquid-filled glass thermometers and thermocouples.[3,4] Therefore, they cannot be applied in submicron scale or harsh environments, such as high-voltage power plants, microcircuits, and intracellular liquids.[5–7] Compared with contact thermometers, optical temperature measurement has the unique advantages of non-contact measurement and large-scale imaging,[8] which are based on particular parameters of luminescence such as the peak position, line width, fluorescence intensity, fluorescence lifetime, and FIR.[9] In particular, FIR from the transitions of thermally coupled levels (TCLs) of rare earth ions can avoid the effects of excitation power fluctuation and spectral loss, leading to a much higher accuracy.

Rare earth doped up-conversion temperature sensing materials based on the FIR from transitions of TCLs have aroused wide interest in the biomedical field owing to their deep penetration depth, being less prone to photobleaching, and exhibiting less spontaneous autofluorescence interference as well as minimal photo damage to living organisms.[10–12] Viruses are small, non-cellular organisms that must be parasitized and replicated in living cells. They are highly infectious and extremely harmful, particularly lentiviruses such as human immunodeficiency virus, and the medical community has not yet found an efficient and reasonable treatment strategy.[13] Recently, researchers have found that lentiviral nucleocapsids play a crucial role in the lentiviral replication cycle and are considered ideal targets for antiviral therapy.[14] Detecting the temperature changes that accompany nucleocapsid binding and exploring the effects of temperature changes on the activity of proteases and reverse transcriptases, helps to deepen the understanding of lentiviral replication and develop more efficient and rational lentiviral treatment strategies. Nano temperature sensors are therefore urgently needed to monitor the temperature changes involved in this process.

For NCs to be used for temperature sensing in biomedicine several main requirements must be met: (i) high UCL efficiency to improve the signal-to-noise ratio; (ii) high stability; (iii) good dispersibility in aqueous solutions; (iv) suitable surface properties, that is, the presence of functional groups such as carboxyl (–COOH), amino ($-NH_2$), or maleimide (MA) groups on the surface to improve the biocompatibility of NCs and allow further conjugation with biological molecules.[12] However, the preparation and application of NC temperature sensors still present numerous challenges. Rare earth doped up-conversion luminescent materials are generally synthesized in liquid conditions by interstitial doping, and the rare earth ions are exposed on the surface of the matrix. When the doping concentration is high, it is easy to cause surface fluorescence quenching, resulting in lower luminescence efficiency.[15] In addition, to control the size and morphology of NCs,

[a]*Key Laboratory of Weak-Light Nonlinear Photonics, Ministry of Education, School of Physics, Nankai University, Tianjin 300071, China. E-mail: zhaolj@nankai.edu.cn; yuhua@nankai.edu.cn*

[b]*TEDA Institute of Biological Sciences and Biotechnology, Nankai University, 23 Hongda Street, TEDA, Tianjin 300457, China*

† Electronic supplementary information (ESI) available. See DOI: 10.1039/c9ra08447a

hydrophobic materials such as oleic acid or oleylamine are often added as capping ligands, so they must be converted into hydrophilic analogues so that they can be applied in biological fields.[16] However, the surface modification process is sensitive to the pH and the amount of ligand as well as other factors, and the capping thickness is not easy to control and can lead to agglomeration.[17,18]

Recently, amphiphilic amino acid biomolecules have received significant attention in the synthesis of water-dispersible NCs in aqueous media as their hydrophilic surface properties make the sample suitable for biotechnology applications.[19] In addition, by using the melting–annealing method, the rare earth ions can be doped into crystallites with low phonon energy by cation substitution, which suppresses the probability of non-radiative relaxation and makes the luminescence efficiency very high.

In this study, we use a conventional melting–annealing method to synthesize GCs, and extract NCs from the GCs by wet chemical etching. While etching, 6AA was modified in the outer layer of nanocrystalline to prevent agglomeration, improve the biocompatibility of NCs and effectively inhibit the energy transfer between RE^{3+} ions and biological tissues. To avoid the interference of spontaneous fluorescence in biological tissues and the thermal damage to living organisms caused by 980 nm lasers, we used a 940 nm laser as the excitation source to study the temperature sensing behavior of the NCs in the liquid environment. Importantly, the Er^{3+}/Yb^{3+} co-doped NCs modified with 6AA have great potential for biomedical application as temperature sensors.

Experimental

Synthesis of Er^{3+}/Yb^{3+} co-doped PbF_2 NCs modified with 6AA

The Er^{3+}/Yb^{3+} co-doped PbF_2 NCs modified with 6AA were prepared using a conventional melting–annealing method with subsequent wet chemical etching. First, the precursor glasses were prepared with the following starting composition ratios (in mol%): $45.5SiO_2$–$40PbF_2$–$10CdF_2$–$0.5Er_2O_3$–$4Yb_2O_3$ *via* the melting–annealing method. The GCs were then obtained from the prepared precursor glasses by thermal treatment for 8 h at 440 °C and then gradually cooled to room temperature. Subsequently, glacial acetic acid and NH_4F in deionized water were mixed to give the etching agent. GC powder was then mixed thoroughly with the as-prepared etching agent and surface-modification agent 6AA with vigorous stirring. Finally, the obtained NCs were collected *via* centrifugation and washed twice with deionized water and ethanol, and dried in an oven at 80 °C for 3 h.

Characterization

The X-ray diffraction (XRD) patterns of samples were measured using a powder diffractometer (D/Max-2500) using CuKα radiation. High-resolution transmission electron microscopy (HRTEM, 2100F, JEOL, Japan) was used to measure the morphology and size of the samples. Fourier transform infrared (FT-IR) spectra (4000–400 cm^{-1}) were recorded for KBr pellets (Thermo Fisher Scientific, USA) containing a powder sample with a NICOLET IS50 FT-IR spectrometer. Raman spectra were measured using a RENISHAW InVia Raman microscope with an excitation laser wavelength of 785 nm. Transmission spectra were recorded using a Hitachi U-4100 UV-visible-NIR spectrophotometer. X-ray photoelectron spectroscopy (XPS) data were collected in an ion-pumped chamber of a photoelectron spectrometer (Kratos Axis-Ultra) equipped with an Al Kα (1486.6 eV) focused X-ray source. Zeta potential was measured with a Brookhaven Instruments ZetaPALS. Steady state UCL spectra were measured using an Edinburgh Instruments FLS920 spectrometer equipped with a 940 nm laser as an excitation source.

Results and discussion

Morphology and structure

The GCs had high luminescence efficiency due to the rare earth ions preferentially precipitating from the glass precursor and being selectively incorporated into the fluoride microcrystals, which have low phonon energies.[20] The structures of β-PbF_2:Er^{3+}/Yb^{3+} GCs and NCs were characterized by XRD. β-PbF_2 has a typical cubic fluorite crystal structure. According to the previous work of the research group,[21–23] rare earth ions replace Pb^{2+} by cation substitution and are compensated by F^- interstitial charge. And at the thermal treatment temperature of 440 °C for 8 h, the glass can be completely crystallized and the crystallinity was the highest, the phase structure of rare earth

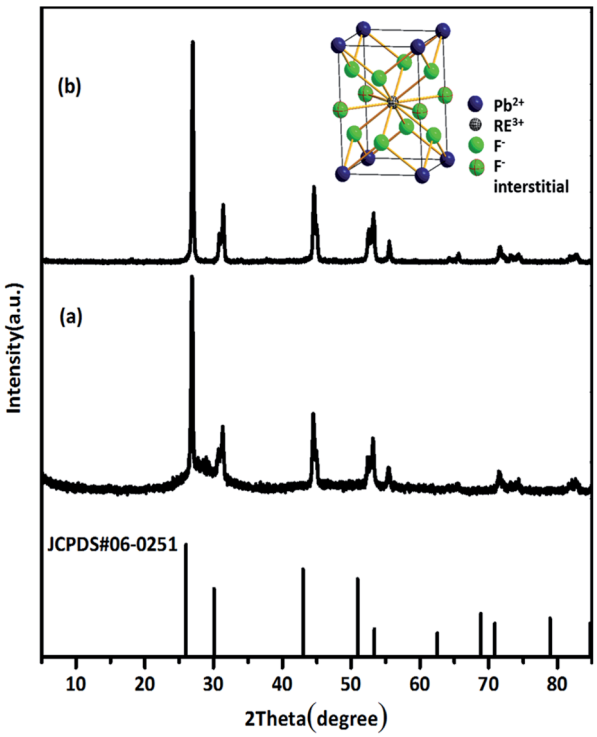

Fig. 1 (a) XRD pattern of GCs (b) XRD pattern of Er^{3+}/Yb^{3+} co-doped β-PbF_2 NCs capped with 6AA. The standard data for β-PbF_2 (PDF #06-0251) is shown for reference. The structure of tetragonal β-PbF_2:RE^{3+} is shown inset.

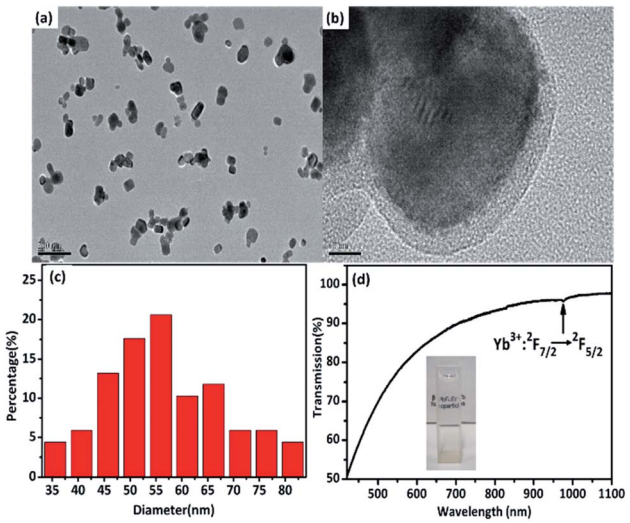

Fig. 2 (a) HRTEM images of NCs modified with 6AA at 200 nm and (b) 20 nm; (c) the size distribution of nanoparticles in aqueous solution; (d) transmission spectrum of the NCs solution. Inset is a photograph of a quartz vessel (10 × 10 × 50 mm^3) filled with the NCs solution.

doped PbF_2 NCs was a tetragonal phase structure, as shown in the inset of Fig. 1. The XRD patterns of the GCs and the NCs released from the GCs were compared with the standard diffraction peaks of β-PbF_2, as shown in Fig. 1(a) and (b). The XRD peak position of the RE^{3+} ion-doped GCs moved to a greater angle, indicating shrinkage of the β-PbF_2 lattice and the incorporation of RE^{3+} ions into the β-PbF_2 crystallite.[24] While, the XRD patterns of the GCs and NCs released from GCs were similar, indicating that the NCs structure remained unchanged during etching.

HRTEM images were used to characterize the morphology of Er^{3+}/Yb^{3+} co-doped PbF_2 NCs, shown in Fig. 2(a) and (b). It can be seen that the dispersion of NCs is good and the average diameter of the NCs is 56 nm. Moreover, it can be clearly seen that the surface of the NCs is modified by a layer of 6AA of approximately 10 nm in thickness. The obtained NCs were capped by the –COOH heads of the bifunctional 6AA molecules with the free $–NH_2$ groups at the opposite end of the molecules being available for further dispersion in polar solvent.[25] As is shown in Fig. 2(d), 6AA modified β-PbF_2:Er^{3+}/Yb^{3+} nanocrystalline solutions are largely transparent to visible light and the absorption peak corresponding to the Yb^{3+}:$^2F_{7/2}$ → $^2F_{5/2}$ transition located at 978 nm can be clearly identified. After adding 6AA, the stability of the solution clearly improved, and the zeta potential increased from +17.7 mV to +32.18 mV, which shows that the NCs have uniform particle size and good dispersion in aqueous solution. Meanwhile, the 6AA coated in the outer layer of NCs has no absorption in this wavelength range, as is shown in Fig. S1.† Therefore, it can effectively inhibit the energy transfer between RE^{3+} ions and biological tissues. The results show that the NCs maintained the phase structure of the GCs and that their surfaces were modified with the bifunctional 6AA ligand, making them potential candidates for biological application.

Etching and surface modification mechanism

A proposed etching and surface modification mechanism is shown in Fig. 3. A schematic diagram of the structure of the

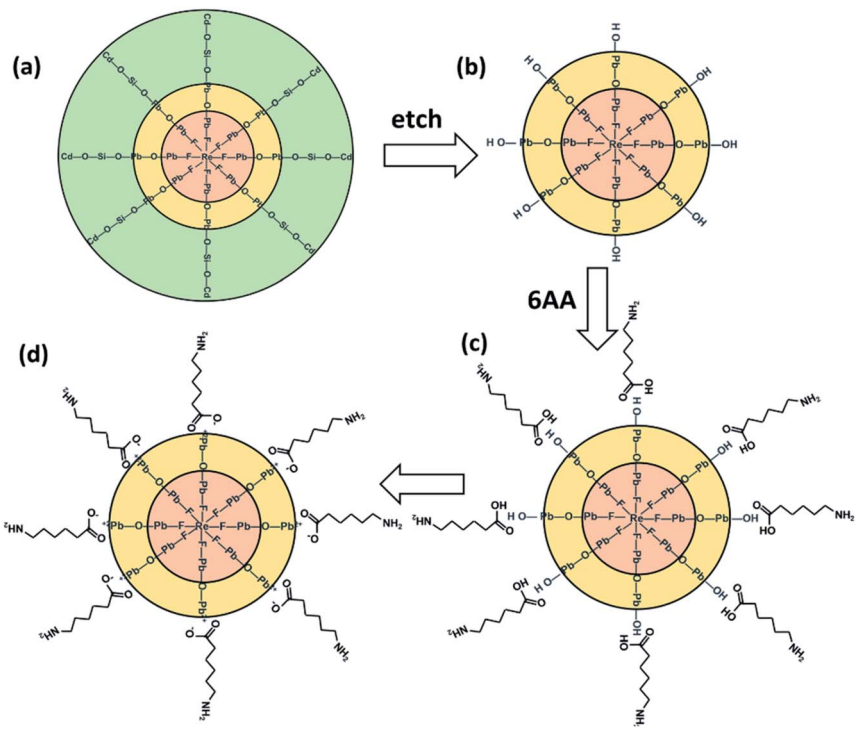

Fig. 3 The schematic diagram of (a) the GCs; (b) the NCs after etching; (c) the NCs react with 6AA; (d) the NCs modified with 6AA.

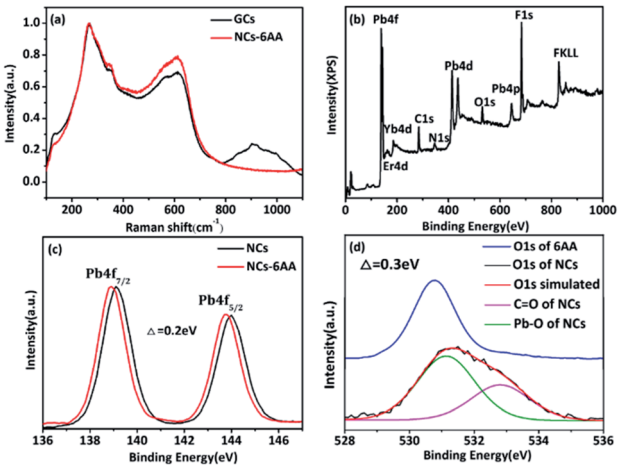

Fig. 4 (a) Raman spectra of GC and NCs capped with 6AA; (b) XPS spectra of NCs modified with 6AA; (c) high-resolution Pb 4f XPS spectra of NCs before and after modification with 6AA; (d) high-resolution O 1s XPS spectra of pure 6AA and NCs modified with 6AA.

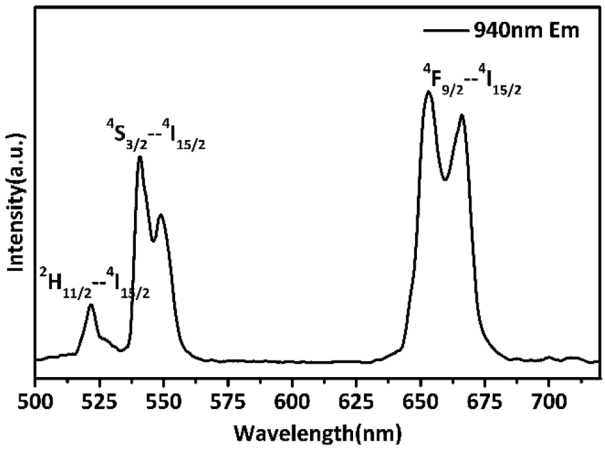

Fig. 5 The up-conversion luminescence spectrum of 6AA capped β-PbF_2:Er^{3+}/Yb^{3+} NCs in aqueous solution under 940 nm laser excitation.

GCs, based on our previous work, is shown in Fig. 3(a).[26] The central structure of the figure is a rare earth fluoride nanocrystal and the outermost layer is a silicon oxide layer, and the two are connected by an intermediate transition layer O–Pb–O bond. When etching occurs, HF generated by the hydrolysis of NH_4F first etches SiO_2 and CdO in the outer layer of the GCs, and then etches the transition layer. The exposed O in the O–Pb–O bond undergoes protonation to become O–Pb–OH. When the etch rate is slow, the contact time of O–Pb–OH with the –COOH group of 6AA is increased, which facilitates the cross-linking reaction of divalent metal ions and removes one water molecule.[27] Thereafter, –COO– and Pb^{2+} are connected by electrostatic adsorption, preventing O–Pb–OOC– from continuing to react with the etchant.

XPS and Raman spectroscopy were used to verify the etching and surface modification model. The Raman spectrum is shown in Fig. 4(a), the low frequency region of 200–400 cm^{-1} is attributed to the vibration of the fluoride,[28] the peak at 256 cm^{-1} belonging to the Pb–F bond vibration, and the vibration at 500–700 cm^{-1} is attributed to the vibration of the Re–F bond.[29] The vibration at 800–1200 cm^{-1} arises as a result of the vibration of the Si–O–Si bond.[30] After etching, the Raman vibration peak of Pb–F at 256 cm^{-1} was still detected, indicating that rare earth doped lead fluoride NCs were preserved. While the vibration peak of the Si–O–Si bond at 800–1200 cm^{-1} was no longer detected, indicating that the silicon oxide of the glass ceramic was completely etched. The XPS spectrum in Fig. 4(b) shows the presence of Pb, F, Er, Yb, C, O, and N. And the high-resolution O 1s, C 1s, and N 1s XPS spectra are shown in Fig. S2.† The peaks at 531.1 eV and 532.1 eV correspond to the characteristic peaks of C=O and Pb–O, respectively.[31,32] The peaks at 284.56 eV, 285.99 eV, and 288.18 eV correspond to the C–C, C–N, and C–C=O,[25,33] respectively. While the peaks at 399.96 eV and 400.78 eV correspond to the characteristic peaks of N–H and N–C, respectively.[34] The XPS spectra indicate that 6AA was present on the surface of the nanocrystal. Fig. 4(c) and (d) shows the high-resolution Pb4f XPS spectra of the NCs before and after modification with 6AA and high-resolution O 1s XPS spectra of pure 6AA. The results show that after being capped with 6AA, the binding energy of Pb 4f moved to lower energy, while the binding energy of C=O in O 1s moved towards higher energy, indicating that the capping with 6AA proceeds through the electron between Pb^{2+} and –COO–,[32] which supports the proposed etching and surface modification model. The etching and surface modification mechanism is also applicable to other amphiphilic amino acid functional ligands.

Up-conversion luminescence and temperature sensing behavior

Yb^{3+} is often used as a sensitizer excited using a 980 nm laser because of its simple energy level structure, large absorption cross section of 980 nm laser light, and high energy transfer efficiency to Er^{3+}, Tm^{3+}, Nd^{3+}, and Ho^{3+}.[35,36] However, the water molecules in the living body strongly absorb 980 nm laser light. The absorption coefficient of water at 980 nm is ~0.485 cm^{-1}.[37] According to the Beer–Lambert law, when 980 nm light propagates 1 cm in water, up to 61% of the light energy is absorbed by the water. Studies have shown that at a laser power density of ~7.6 W cm^{-2}, the temperature of the water rises by ~18 °C after 15 min of irradiation.[38] This thermal effect can induce cell and tissue damage and affect the accuracy of temperature measurement.[39] To prevent thermal damage to the organism by the 980 nm laser, a 940 nm laser was used as the excitation source.

Fig. 5 shows the up-conversion luminescence spectrum of β-PbF_2:Er^{3+}/Yb^{3+} NCs in aqueous solution under 940 nm laser excitation. Using the melting–annealing method, rare earth ions can be doped into crystallites with low phonon energy by body-doping and the luminescence efficiency is higher. The spectrum shows two characteristic emission bands for green light at 521 and 540 nm and red light at 660 nm, resulting from the $^2H_{11/2} \rightarrow {}^4S_{3/2}$, $^4I_{15/2}$, and $^4F_{9/2} \rightarrow {}^4I_{15/2}$ energy level transitions of Er^{3+}, respectively.

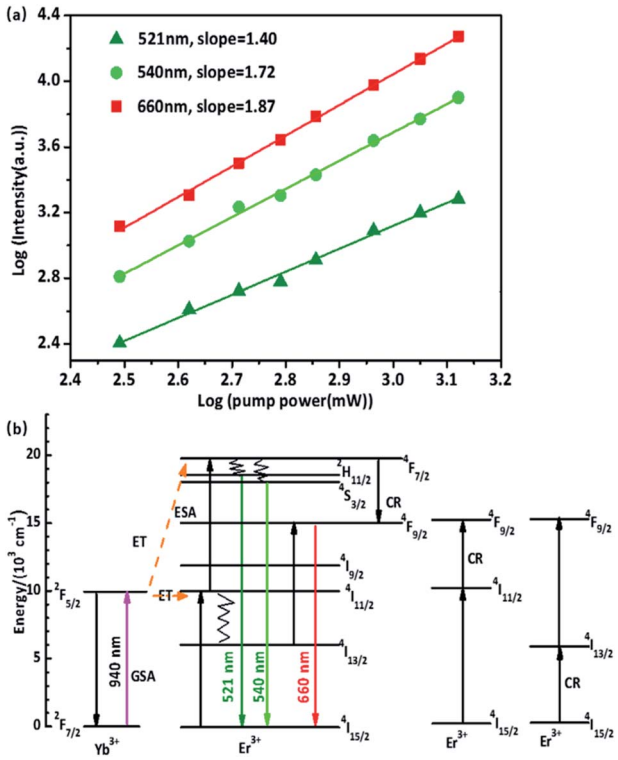

Fig. 6 (a) Log–log plots of intensity and pumping power for 521, 540, and 660 nm emissions at room temperature; (b) energy-level diagram for Er^{3+}/Yb^{3+} co-doped β-PbF_2 NCs modified with 6AA and the possible up-conversion mechanisms.

Up-conversion luminescence is a multiphoton absorption process. The relationship between the up-conversion luminescence intensity and pump power is: $I_{em} \propto (P_{pump})^n$, where I_{em} is the up-conversion luminescence intensity, P_{pump} is the excitation optical pump power, and n is the number of pump photons populated to the upper level.[40] Taking the logarithm of both sides, the relationship between lg I_{em} and lg P_{pump} is obtained, which gives the *P–I* curve, and the slope of the curve is the value of n. The *P–I* curve of the nanocrystal solution is shown in Fig. 6(a), and the slopes at 521, 540, and 660 nm were approximately 1.40, 1.72, and 1.87, respectively. The results show that red and green up-conversion emission are both two-photon up-conversion processes under 940 nm excitation.

A possible up-conversion mechanism for the investigated system is proposed and illustrated in Fig. 6(b) based on the results mentioned above. Under 940 nm excitation, the electrons of the Yb^{3+} ion are excited from the $^2F_{7/2}$ level to the $^2F_{5/2}$ level through ground-state absorption (GSA). Then, the excited Yb^{3+} ions donate as-absorbed energy to adjacent Er^{3+} ions and the Er^{3+} ions are excited from the $^4I_{15/2}$ level to the $^4I_{11/2}$ level. A second 940 nm photon transferred by the adjacent Yb^{3+} ions can excite Er^{3+} ions from the $^4F_{11/2}$ to $^4F_{7/2}$ level by the two photons process, and finally through nonradiative relaxations to $^2H_{11/2}$, $^4S_{3/2}$, emitting 521 nm and 540 nm photons, respectively. This is the up-conversion luminescence mechanism of green emission. There are four possible mechanisms for the red emission: (i) from $^2H_{11/2}/^4S_{3/2}$ through nonradiative relaxations

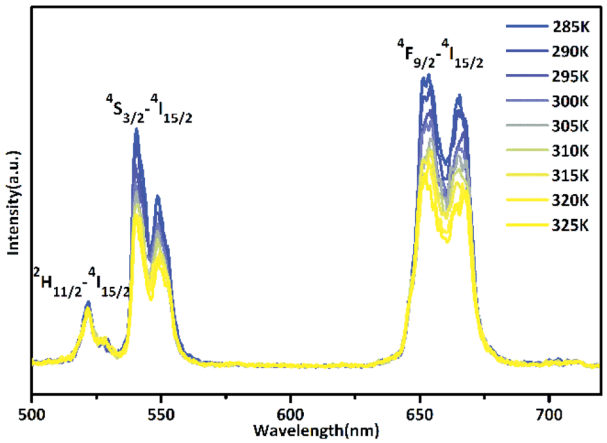

Fig. 7 Temperature dependent spectrum of Er^{3+} green and red emissions of 6AA capped β-PbF_2:Er^{3+}/Yb^{3+} nanocrystalline solution.

to $^4F_{9/2}$, the energy level difference between the two energy levels is 3200 cm^{-1}, which is approximately 14 phonons energy of β-PbF_2. It is generally thought that this is non-radiative relaxation, however, after coating with 6AA, the phonon energy of the surface groups is ~3350 cm^{-1}, as shown in Fig. S1,† which matches the difference between $^2H_{11/2}/^4S_{3/2}$ and $^4F_{9/2}$, therefore a 660 nm photon is emitted. (ii) The electrons of the Yb^{3+} are excited from the $^2F_{7/2}$ level to the $^2F_{5/2}$ level through ground-state absorption (GSA), and the Yb^{3+} ion transfers energy to the Er^{3+} ion, causing Er^{3+} to be excited from the $^4I_{15/2}$ level to the $^4I_{11/2}$ level. Since the $^4I_{13/2}$ energy level has a long lifetime and the energy level difference matches the phonon energy of the 6AA surface group, some of the photons relax to $^4I_{13/2}$. The electrons in the $^4I_{13/2}$ level are excited to the $^4F_{9/2}$ level by absorbing the energy transferred by the Yb^{3+} ion or the GSA, and then return to the ground state $^4I_{15/2}$, emitting a 660 nm photon. (iii) and (iv) The electrons in the $^4F_{7/2}$ energy level relax to the $^4F_{9/2}$ level by cross-relaxation with the adjacent Er^{3+} ions. Subsequently, radiative transfer from the $^4F_{9/2}$ to $^4I_{15/2}$ levels results in red emission.

The up-conversion emission spectrum of the sample in the wavelength range 500–720 nm at different temperatures under 940 nm irradiation is presented in Fig. 7, the pump power of the 940 nm laser was set at 120 mW mm^{-2}. $^2H_{11/2}$ and $^4S_{3/2}$ are the thermal coupling levels. of Er^{3+}, and the number of particles at this level obeys the Boltzmann particle distribution. The intensity of the emitted fluorescence is proportional to the number of particles in the energy level, therefore the FIR emitted by the thermal coupling level can be given as follows:[29]

$$\mathrm{FIR} = \frac{N_2}{N_1} = \frac{I_{2j}}{I_{1j}} = \frac{g_2\sigma_{2j}\omega_{2j}}{g_1\sigma_{1j}\omega_{1j}} \exp\left(-\frac{\Delta E}{k_B T}\right) = B \exp\left(-\frac{\Delta E}{k_B T}\right) \quad (1)$$

where N_{ij}, I_{ij}, g_{ij}, σ_{ij}, and ω_{ij} represent the number of ions, fluorescence intensity, degeneracy, emission cross section, and fluorescence emission angular frequency for the transition of $^2H_{11/2} \rightarrow {}^4I_{15/2}$ and $^4S_{3/2} \rightarrow {}^4I_{15/2}$, respectively. ΔE is the

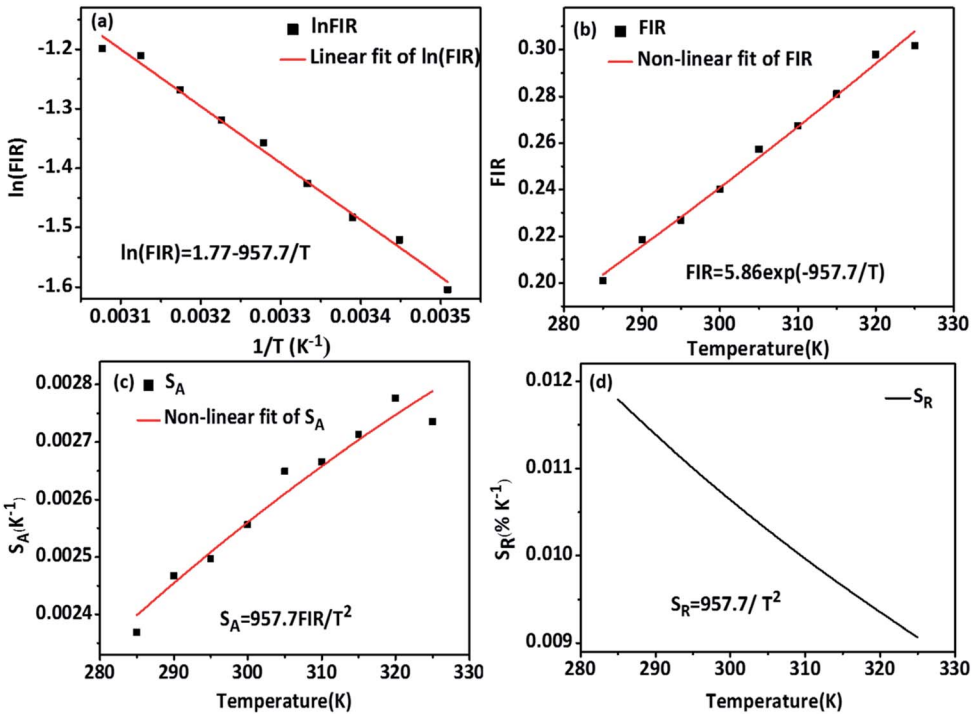

Fig. 8 (a) Monolog plot of FIR ($^2H_{11/2}/^4S_{3/2}$) as a function of inverse absolute temperature; (b) the evolution of FIR ($^2H_{11/2}/^4S_{3/2}$) with temperature; (c) the absolute sensitivity as a function of temperature; (d) the relative sensitivity as a function of temperature.

difference between $^2H_{11/2}$ and $^4S_{3/2}$, k_B is the Boltzmann constant, and T is the absolute temperature. The logarithm of the above formula is obtained:

$$\ln(\mathrm{FIR}) = \ln B - \frac{\Delta E}{k_B T} \quad (2)$$

and the fluorescence intensity ratio is logarithmically matched to the reciprocal of temperature, the slope value and the intercept value are $\Delta E/k_B = 957.7$ and $\ln B = 1.77$, respectively. The change in fluorescence intensity ratio with temperature can be fitted by eqn (2), and the fitting results are shown in Fig. 8(a) and (b).

Sensitivity and resolution are important parameters for the application of the system as an optical temperature sensor. Sensitivity is used to characterize the fluorescence intensity ratio as a function of temperature. Absolute sensitivity S_A and relative sensitivity S_R are defined as:[48,49]

$$S_A = \frac{d\mathrm{FIR}}{dT} = \mathrm{FIR}\left(\frac{\Delta E}{k_B T^2}\right) \quad (3)$$

$$S_R = \frac{1}{\mathrm{FIR}}\frac{d\mathrm{FIR}}{dT} = \frac{\Delta E}{k_B T^2} \quad (4)$$

Based on the above formulas, the absolute sensitivity S_A and relative sensitivity S_R of β-PbF_2:Er^{3+}/Yb^{3+} nanocrystals are shown in Fig. 8(c) and (d), and the maximum values were 0.0027 K^{-1} (325 K) and 1.18% K^{-1} (285 K), respectively. The temperature resolution (δT) is used to characterize the smallest temperature change that can be detected and depends on the

Table 1 The absolute sensitivity, relative sensitivity and resolution of optical thermometers based on fluorescence intensity ratio of green emission from the transitions of TCLs ($^2H_{11/2}/^4S_{3/2}$) of Er^{3+}

Material	Temperature range (K)	λ_{ex} (nm)	S_{Rmax} (% K^{-1})	S_{Amax} (10^{-3} K^{-1})	δT (K)	Ref.
$GdVO_4$:Er^{3+}/Yb^{3+}	297–343	980	0.94	10.1	0.4	41
β-$NaLuF_4$:Yb^{3+}, Tm^{3+}, Er^{3+}	300–600	980		7.7		42
$NaZnPO_4$:Er^{3+}/Yb^{3+} GCs	303–753	980	1.329	5.7		43
Fluoride glass:Er^{3+}/Yb^{3+}	335–375	975	1.1	0.87	0.8	44
Silica glass:Er^{3+}/Yb^{3+}	296–723	978	1.09	3.3	0.2	45
$Ca_5(PO_4)_3F$:Er^{3+}/Yb^{3+} GCs	298–798	980	1.35	5.19		46
$NaYF_4$:Er^{3+}/Yb^{3+}	299–336	920	1.0			47
Borophosphate:Er^{3+}/Yb^{3+}	298–798	980	1.66	4.5		48
β-PbF_2:Er^{3+}/Yb^{3+} NCs	285–325	940	1.18	2.7	0.25	This work

system performance (given by the relative sensitivity) and experimental setup. δT is calculated using the following equation:[49,50]

$$\delta T = \frac{1}{S_R}\frac{\delta \Delta}{\Delta} \quad (5)$$

where Δ is the thermometric parameter used in the temperature probing at a certain temperature, herein, Δ is FIR. $\delta\Delta$ is the standard deviation value of the FIR at a given temperature, calculated by the formula:

$$\delta \Delta = \sqrt{\frac{1}{n-1}\sum_{i=1}^{n}(\mathrm{FIR} - \overline{\mathrm{FIR}})^2} \quad (6)$$

where $\overline{\mathrm{FIR}}$ is the average of the FIR, obtained by five times measurement of one sample at each temperature, and herein $n = 5$. Corresponding to the relative sensitivity of each temperature, we calculate the resolution at each temperature and the averaged resolution is about 0.25 K. Compared to the other optical thermometers based on fluorescence intensity ratio of green emission from the transitions of TCLs ($^2H_{11/2}/^4S_{3/2}$) of Er^{3+} is listed in Table 1. The high sensitivity and resolution indicate that β-PbF_2:Er^{3+}/Yb^{3+} nanocrystals have potential for use as a nano-fluorescence temperature sensor.

Conclusions

β-PbF_2:Er^{3+}/Yb^{3+} NCs modified with 6AA were prepared by etching the glass matrix of GCs and modified with bifunctional 6AA ligands. The NCs were largely transparent and stable in aqueous solution. Under the excitation of a 940 nm laser the NCs displayed efficient green and red emission without requiring 980 nm laser excitation, which has a heating effect on living organisms. The fluorescence intensity ratio of green emission from the transitions of TCLs ($^2H_{11/2}/^4S_{3/2}$) of Er^{3+} were used for biological temperature sensing based on the FIR technique and we obtained high sensitivity and resolution in the biological temperature range. The described results indicate that the β-PbF_2:Er^{3+}/Yb^{3+} NCs modified with 6AA are promising candidates for use as accurate optical temperature sensors in the biomedical field.

Conflicts of interest

There are no conflicts to declare.

Acknowledgements

This work was supported by the National Natural Science Foundation of China (No. 11574164 and No. 31870158), 111 Project (No. B07013) and National Science Fund for Talent Training in the Basic Sciences (No. J1103208).

Notes and references

1 X. D. Wang, O. S. Wolfbeis and R. J. Meier, *Chem. Soc. Rev.*, 2013, **42**, 7834–7869.
2 X. Wang, Q. Liu, Y. Bu, C. S. Liu, T. Liu and X. Yan, *RSC Adv.*, 2015, **5**, 86219–86236.
3 L. Michalski, K. Eckersdorf, J. Kucharski and J. McGhee, *Temperature Measurement*, Wiley, United States, 2nd edn, 2002.
4 N. W. Ashcroft and D. N. Mermin, *Phys. Today*, 1977, **30**, 61–65.
5 R. Bogue and J. Newman, *Sens. Rev.*, 2007, **27**, 86–90.
6 L. Guo, W. Dong and S. Zhang, *RSC Adv.*, 2014, **4**, 41956–41967.
7 N. Armaroli and V. Balzani, *Energy Environ. Sci.*, 2011, **4**, 3193–3222.
8 C. Gunawan, M. Lim, C. P. Marquis and R. Amal, *J. Mater. Chem. B*, 2014, **2**, 2060–2083.
9 D. Jaque and F. Vetrone, *Nanoscale*, 2012, **4**, 4301–4326.
10 H. S. Mader, P. Kele, S. M. Saleh and O. S. Wolfbeis, *Curr. Opin. Chem. Biol.*, 2010, **14**, 582–596.
11 D. E. Achatz, R. Ali and O. S. Wolfbeis, *Top. Curr. Chem.*, 2011, **300**, 29.
12 J. Zhou, Z. Liu and F. Y. Li, *Chem. Soc. Rev.*, 2012, **41**, 1323–1349.
13 M. Nag, K. D. Paris and J. E. Fogle, *Viruses*, 2018, **10**, 227.
14 M. Mori, L. Kovalenko, S. Lyonnais, D. Antaki, B. E. Torbett, M. Botta, G. Mirambeau and Y. Mély, *Curr. Top. Microbiol. Immunol.*, 2015, **389**, 53.
15 H. Qiu, L. Sun, S. Tan, Y. Sun, S. Hao, Y. Yu, W. Lu, S. Ge and C. Yang, *J. Nanosci. Nanotechnol.*, 2011, **11**, 7700.
16 H. P. Zhou, C. H. Xu, W. Sun and C. H. Yan, *Adv. Funct. Mater.*, 2010, **19**, 3892–3900.
17 A. Hlaváček, A. Sedlmeier, P. Skládal and H. H. Gorris, *ACS Appl. Mater. Interfaces*, 2014, **6**, 6930.
18 H. Chang, J. Xie, B. Zhao, B. Liu, S. Xu, R. Na, X. Xie, H. Ling and H. Wei, *Nanomaterials*, 2015, **5**, 1–25.
19 F. C. Meldrum and C. L. Helmut, *Chem. Rev.*, 2008, **108**, 4332–4432.
20 Y. Wang and J. Ohwaki, *Appl. Phys. Lett.*, 1998, **63**, 3268–3270.
21 N. Hu, H. Yu, M. Zhang, P. Zhang, Y. Z. Wang and L. J. Zhao, *Phys. Chem. Chem. Phys.*, 2011, **13**, 1499–1505.
22 J. Ge, L. J. Zhao, H. Guo, Z. J. Lan and H. Yu, *Phys. Chem. Chem. Phys.*, 2013, **15**, 17281–17286.
23 H. Yu, K. D. Zhou, K. Chen, J. Song, C. X. Hou and L. J. Zhao, *J. Non-Cryst. Solids*, 2008, **354**, 3649–3652.
24 V. K. Tikhomirov, D. Furniss, A. B. Seddon, I. M. Reaney, M. Beggiora, M. Ferrari, M. Montagna and R. Rolli, *Appl. Phys. Lett.*, 2002, **81**, 1937–1939.
25 T. D. Nguyen, D. Mrabet and C. T. Dinh, *CrystEngComm*, 2011, **13**, 1450–1460.
26 M. Liu, L. J. Zhao, Y. Liu, Z. J. Lan, L. F. Chang, Y. M. Li and H. Yu, *J. Mater. Sci. Technol.*, 2014, **30**, 1213–1216.
27 T. Sugama, L. E. Kukacka and N. Carciello, *J. Mater. Sci.*, 1984, **19**, 4045–4056.
28 P. McMillan and B. Piriou, *J. Non-Cryst. Solids*, 1983, **55**, 221–242.
29 W. R. Wilmarth, G. M. Begun, S. E. Nave and J. R. Peterson, *J. Chem. Phys.*, 1998, **89**, 711.
30 S. A. Brawer and W. B. White, *J. Chem. Phys.*, 1975, **63**, 2421.

31 S. W. Han, S. W. Joo, T. H. Ha, Y. Kim and K. Kim, *J. Chem. Phys.*, 2000, **104**(50), 11987–11995.
32 X. Zhao, Y. Wang, Y. Li, W. Xue, J. Li, H. Wu, Y. Zhang, B. Li, W. Liu, Z. Gao and H. Huang, *J. Chem. Eng. Data*, 2019, **64**(6), 2728–2735.
33 L. Zhang, F. Song, Y. Wu, L. Cheng, J. Qian, S. Wang, Q. Chen and Y. Li, *J. Chem. Eng. Data*, 2019, **64**, 176–188.
34 C. Jin, X. Zhang, J. Xin, G. Liu and Z. Kong, *Ind. Eng. Chem. Res.*, 2018, **57**, 7872–7880.
35 F. Wang and X. G. Liu, *Chem. Soc. Rev.*, 2009, **38**, 976–989.
36 S. Wen, J. Zhou, K. Zheng, A. Bednarkiewicz, X. Liu and D. Jin, *Nat. Commun.*, 2018, **9**(1), 2415.
37 M. J. Weber, *Phys. Rev. B: Condens. Matter Mater. Phys.*, 1971, **4**, 3153–3159.
38 Q. Shao, Z. Yang, G. Zhang, Y. Hu and J. Jiang, *ACS Omega*, 2018, **3**, 188–197.
39 Z. Qiuqiang, Q. Jun, L. Huijuan, S. Gabriel, W. Dan, H. Sailing, Z. Zhiguo and A. E. Stefan, *ACS Nano*, 2011, **5**, 3744–3757.
40 M. Pollnau, D. R. Gamelin, S. R. Lüthi, H. U. Güdel and M. P. Hehlen, *Phys. Rev. B: Condens. Matter Mater. Phys.*, 2000, **61**, 3337–3346.
41 O. Savchuk, J. J. Carvajal, C. Cascales, M. Aguilo and F. Diaz, *ACS Appl. Mater. Interfaces*, 2016, **8**, 7266–7273.
42 H. Lu, H. Hao, G. Shi, Y. Gao, R. Wang, Y. Song, Y. Wang and X. Zhang, *RSC Adv.*, 2016, **6**, 55307.
43 Y. Chen, G. H. Chen, X. Y. Liu and T. Yang, *J. Lumin.*, 2018, **195**, 314–320.
44 E. Saïdi, B. Samson, L. Aigouy, S. Volz, P. Löw, C. Bergaud and M. Mortier, *Nanotechnology*, 2009, **20**, 115703.
45 C. Li, B. Dong, S. Li and C. Song, *Chem. Phys. Lett.*, 2007, **443**, 426–449.
46 X. Liu, Y. Chen, F. Shang, G. Chen and J. Xu, *J. Mater. Sci.: Mater. Electron.*, 2019, **30**, 5718–5725.
47 F. Vetrone, R. Naccache, A. Zamarrón, A. Juarranz de la Fuente, F. Sanz-Rodríguez, L. Martinez Maestro, E. Martín Rodriguez, D. Jaque, J. García Solé and J. A. Capobianco, *ACS Nano*, 2010, **4**, 3254–3258.
48 S. A. Wade, S. F. Collins and G. W. Baxter, *J. Appl. Phys.*, 2003, **94**, 4743–4756.
49 S. Uchiyama, T. Tsuji, K. Ikado, A. Yoshida, K. Kawamoto, T. Hayashi and N. Inada, *Analyst*, 2015, **140**, 4498–4506.
50 C. D. S. Brites, A. Millán and L. D. Carlos, *Handb. Phys. Chem. Rare Earths*, 2016, **49**, 339–427.